J. Fluid Mech. (1982), *vol.* 119, *pp.* 507–532
Printed in Great Britain

Numerical studies of surface-tension effects in nonlinear Kelvin–Helmholtz and Rayleigh–Taylor instability

By D. I. PULLIN

Department of Mechanical Engineering, University of Melbourne, Parkville 3052, Victoria, Australia

(Received 5 January 1981 and in revised form 9 November 1981)

We consider the behaviour of an interface between two immiscible inviscid incompressible fluids of different density moving under the action of gravity, inertial and interfacial tension forces. A vortex-sheet model of the exact nonlinear two-dimensional motion of this interface is formulated which includes expressions for an appropriate set of integral invariants. A numerical method for solving the vortex-sheet initial-value equations is developed, and is used to study the nonlinear growth of finite-amplitude normal modes for both Kelvin–Helmholtz and Rayleigh–Taylor instability. In the absence of an interfacial or surface-tension term in the integral–differential equation that describes the evolution of the circulation distribution on the vortex sheet, it is found that chaotic motion of, or the appearance of curvature singularities in, the discretized interface profiles prevent the simulations from proceeding to the late-time highly nonlinear phase of the motion. This unphysical behaviour is interpreted as a numerical manifestation of possible ill-posedness in the initial-value equations equivalent to the infinite growth rate of infinitesimal-wavelength disturbances in the linearized stability theory. The inclusion of an interfacial tension term in the circulation equation (which stabilizes linearized short-wavelength perturbations) was found to smooth profile irregularities but only for finite times. While coherent interfacial motion could then be followed well into the nonlinear regime for both the Kelvin–Helmholtz and Rayleigh–Taylor modes, locally irregular behaviour eventually reappeared and resisted subsequent attempts at numerical smoothing or suppression. Although several numerical and/or physical mechanisms are discussed that might produce irregular behaviour of the discretized interface in the presence of an interfacial-tension term, the basic cause of this instability remains unknown. The final description of the nonlinear interface motion thus awaits further research.

1. Introduction

The problem of the nonlinear stability of an interface between two fluids of different density remains a considerable challenge to mathematicians and numerical analysts alike. If the heavier fluid lies above the lighter fluid, then under the action of the destabilizing force of gravity the interface may be subject to Rayleigh–Taylor instability (see Taylor 1950) resulting in the characteristic spike–bubble interfacial shape pattern as the interface amplitude grows exponentially with time. When the lighter fluid is

† Present address: Department of Mechanical Engineering, University of Queensland, St Lucia, 4067, Queensland, Australia.

above, the configuration is statically stable, but the superposition of a velocity difference across the interface can generate inertially induced Kelvin–Helmholtz instability (Kelvin 1910). If the two fluids are both incompressible and inviscid then in the absence of surface tension the linearized theory of both these instability modes predicts that the growth rate of disturbances increases without limit with decreasing wavelength. In real fluids this behaviour is modified by the stabilizing action of both interfacial (surface) tension and viscosity. For the inviscid Kelvin–Helmholtz mode, the action of surface tension is sufficient to inhibit the onset of (linearized) instability at all wavelengths for values of the velocity difference that do not exceed a certain critical value (Chandrasekhar 1961). Greater velocity differences lead to instability, but only for wavelengths above a certain minimum value which depends on both the velocity difference and the fluid properties. In the (linearized) Rayleigh–Taylor mode, surface tension stabilizes interfacial perturbations at all wavelengths below a critical value that depends only on fluid properties (Chandrasekhar 1961; Bellman & Pennington 1954).

In an effort to proceed beyond the range of validity of the linearized theories, various numerical methods have been applied to the interfacial-stability problem and to related phenomena such as nonlinear free-surface wave behaviour. For Rayleigh–Taylor instability these have included numerical solutions of the time-dependent Navier–Stokes equations (Harlow & Welch 1966; Daly 1967, 1969; Hirt, Cook & Butler 1970), at least one of which (Daly 1969) shows the effect of surface tension on the late-time formation of a heavy-fluid spike for cylindrical geometry. Earlier, Birkhoff (1962) showed that two-dimensional inviscid interfacial motion could be formulated in terms of variables describing the shape and circulation distribution of a vortex sheet representing the interface, thus reducing the effective space dimensionality of the problem by one. At the same time Birkhoff argued that without the smoothing effect of surface tension and/or viscosity, the subsequent nonlinear initial-value problem may be ill-posed, in view of the unbounded growth rate at decreasing wavelength in the linear analysis. Since surface tension removes the ill-posedness in the linear theory he suggested that it may do likewise in the nonlinear case, although no proof was given.

For the much studied and special case of vortex-sheet motion in a constant-density fluid (as a shear-layer model) surface tension cannot generally be introduced on physical grounds – although there is no reason why it could not be used as an artificial smoothing method – so that questions associated with ill-posedness remain. The first numerical study of this problem was that of Rosenhead (1931) who modelled the vortex sheet by a row of point vortices whose mutually self-inductive motion was supposed to approximate the true vortex-sheet motion. Unfortunately both Rosenhead and later workers found that chaotic or 'turbulent' behaviour of the vortices resulted in regions where smooth roll-up of the vortex sheet might otherwise have been expected. In the half-century following Rosenhead's work, the cause of this behaviour and its possible remedy have been the subject of intense debate. Three possible explanations have emerged:

(*a*) the chaotic motion is a result of inadequate resolution in regions of high curvature (i.e. more vortices are needed), or of the use of an unstable time-stepping procedure;

(*b*) it is a result of the crudeness of the point-vortex model as an approximation to the Cauchy principal value (CPV) integral that expresses the self-induced motion of a continuous vortex sheet;

(*c*) it is a discrete numerical equivalent of the linearized infinitesimal-wavelength instability.

Of the above, (*a*) has been discounted in a careful study by Moore (1974). In considering (*b*), Fink & Soh (1978) showed that terms proportional to the logarithm of the local point-vortex spacing are neglected in the point-vortex model. They proposed a method of redistributing the vortices at each time step which eliminated this error and which appeared to check the onset of chaotic motion. Baker (1980), however, showed subsequently that Fink & Soh neglect curvature terms in the CPV integral calculation, which leads to further errors. He demonstrated that accurate calculation of the integral by subtracting off the singularity did not lead to smooth behaviour. A similar conclusion was reached independently by van de Vooren (1980). Moore (1980) presents a very strong case for (*c*) by detailed examination of the special case of a uniform circular vortex sheet. Through a combination of spectral analysis of the growing numerical error and analytical study of discrete-model behaviour Moore concludes that the mechanism of chaotic motion is indeed a discrete form of Helmholtz instability. The re-positioning method of Fink & Soh and a linear-smoothing technique used by Longuet-Higgins & Cokelet (1976) to suppress a saw-tooth-like instability in related free-surface flows are interpreted as *ad hoc* but effective means of inhibiting growth of the error. The possible counterpart of the instability in a continuous vortex sheet was suggested to be the spontaneous growth of a curvature singularity (Moore 1979).

Extensions of vortex-sheet-like formulations of interfacial motion to the case of a finite-density discontinuity have been developed by several authors. Zaroodny & Greenberg (1973) applied this method to free-surface-wave behaviour. They did not include a surface-tension term, but, since this flow is not subject to linearized short-wavelength inertial instability, the problem of ill-posedness is not critical. The same applies to the study by Longuet-Higgins & Cokelet (1976) of forced breaking waves, at least before the wave overturns. The cause of their observed saw-tooth-like instability is unknown but, for the reason given above, it seems unlikely that it is physically based. Baker, Meiron & Orszag (1980) do not include surface tension in their vortex study of Rayleigh–Taylor instability, but did not encounter difficulties associated with the short-wavelength problem. Their results do not agree with those of the present study for the same flow. Zalosh (1976) appears to have been the first to include surface tension in a vortex-type treatment of interfacial motion. Using the simple point-vortex model to study Kelvin–Helmholtz instability, Zalosh found that, for unstable conditions, irregularities developed on the interface profile where some form of coherent roll-up might be expected. The possible relationship of this behaviour to chaotic motion in the constant-density case or to the saw-tooth instability in the other extreme of free-surface flow remains an unanswered question.

In the present paper we develop a vortex-sheet formulation for the inviscid–incompressible two-fluid interfacial problem. In § 2 the initial-value equations describing the motion of the density interface are derived. The equation for the evolution of the circulation distribution is one order of differentiation (along the interface) less than in the formulations of Birkhoff (1962), Zalosh (1976) and Baker *et al.* (1980), thus allowing a somewhat more direct treatment of interfacial tension terms. A numerical method for the solution of the initial-value equations is developed in § 3. The troublesome CPV integrals are treated by subtraction of the singularity so that curvature terms are included. In § 4 the method is applied to Kelvin–Helmholtz instability at

Froude numbers of order unity, while in §5 it is used to study Rayleigh–Taylor instability. The results of these simulations are discussed in §6, and the main conclusions drawn are summarized in §7.

2. Nonlinear equations for the interface motion

Consider the two-dimensional motion of two immiscible, incompressible, inviscid fluids separated by an interface. We choose rectangular co-ordinates (X, Y), with the X-axis horizontal and aligned with initial mean level of the interface, and the Y-axis vertical. The local gravitational field with acceleration due to gravity g acts in the negative Y-direction. We use the subscripts 1 and 2 to denote fluid properties below and above the interface respectively. The fluid densities are $\tilde{\rho}_1$ and $\tilde{\rho}_2$ while the constant X-velocities far from the interface are $\tilde{U}_1$ $(Y \to -\infty)$, $\tilde{U}_2$ $(Y \to \infty)$. The interfacial shape is assumed to be periodic in the X-direction with wavelength λ. Units of length, time and mass are chosen respectively as λ/π, $(\lambda/g\pi)^{\frac{1}{2}}$ and $\frac{1}{2}(\tilde{\rho}_1+\tilde{\rho}_2)(\lambda/\pi)^3$ and, except where otherwise stated, all quantities shall be non-dimensionalized with respect to these scales.

For later convenience we shall work in a framework such that $\tilde{\rho}_1\tilde{U}_1+\tilde{\rho}_2\tilde{U}_2 = 0$. When the Froude number F is defined as

$$F = \frac{\tilde{U}_1-\tilde{U}_2}{(\lambda g)^{\frac{1}{2}}}, \tag{1}$$

it then follows that the dimensionless velocity at infinity and the density in the fluid 1 are respectively

$$U_1 = \tfrac{1}{2}(1-\alpha)\pi^{\frac{1}{2}}F, \quad \rho_1 = 1+\alpha, \tag{2a}$$

while the corresponding quantities in the fluid 2 are

$$U_2 = -\tfrac{1}{2}(1+\alpha)\pi^{\frac{1}{2}}F, \quad \rho_2 = 1-\alpha, \tag{2b}$$

where

$$\alpha = \frac{\rho_1-\rho_2}{\rho_1+\rho_2}. \tag{3}$$

We seek a description of the two-fluid motion in terms of the motion of a single wavelength of the interface, which we denote by C. As independent variables we take the time t and a parameter a that labels a particular marker particle moving on C in a fashion to be described subsequently. The shape of C at any t is given by the complex function $z(a,t) = x(a,t)+iy(a,t)$. For a single wavelength of length π we arbitrarily take $\frac{1}{2}\pi \geqslant a > -\frac{1}{2}\pi$, so that X-wise periodicity implies

$$z(a+\pi,t) = z(a,t)+\pi, \tag{4}$$

2.1. *Complex velocity field*

The fluid motion is assumed to be two-dimensional, and to start from initial conditions to be specified under the action of gravity, surface tension, pressure and inertial forces only, so that except on C it may be thus taken to be irrotational for all $t \geqslant 0$. Hence we may define a complex velocity potential $W = \phi+i\psi$ on each side of C, where ϕ and ψ are the velocity potential and stream function respectively. An expression for W valid

throughout both fluids may be constructed through a distribution of vortex-like singularities on C. We thus introduce Birkhoff's (1962) circulation co-ordinate $\Gamma(a,t)$, which we define here as the cumulative circulation between a point labelled by a on C and the arbitrarily chosen point $a = \frac{1}{2}\pi$. Milne-Thomson (1968) obtains expressions for W and for the complex velocity dW/dZ induced by an infinite, periodic array of point vortices. Expressions for corresponding quantities at a general point $Z = X + iY$ in either fluid due to the present periodic but continuous singularity distribution (vortex sheet) may be developed through a simple extension of Milne-Thomson's results to yield

$$W(Z,t) = \frac{1}{2\pi i}\int_{-\frac{1}{2}\pi}^{\frac{1}{2}\pi} \log[\sin(Z-z')]\frac{\partial\Gamma'}{\partial a'}da' + \bar{U}Z, \tag{5}$$

$$\frac{dW}{dZ} = \frac{1}{2\pi i}\int_{-\frac{1}{2}\pi}^{\frac{1}{2}\pi} \cot(Z-z')\frac{\partial\Gamma'}{\partial a'}da' + \bar{U}, \tag{6}$$

where $\bar{U} = \frac{1}{2}(U_1 + U_2)$ is the uniform convection velocity, $z' = z(a',t)$ and $\Gamma' = \Gamma(a',t)$. Expanding the integral in (6) for $Y \to \pm\infty$, and comparing the resulting asymptotic X-velocities with (2) then shows that, since by definition $\Gamma(\frac{1}{2}\pi,t) = 0$, we must have $\Gamma(-\frac{1}{2}\pi,t) = -\pi(U_1 - U_2) = -\pi^{\frac{3}{2}}F$, independent of t. Hence $\Gamma(a,t)$ satisfies

$$\Gamma(a+\pi,t) = \Gamma(a) + \pi^{\frac{3}{2}}F. \tag{7}$$

Equations (4) and (7) show that

$$z(a,t) - a, \quad \Gamma(a,t) - \pi^{\frac{1}{2}}Fa \tag{8}$$

must always remain periodic functions of a.

2.2. *Equations for $z(a,t)$ and $\Gamma(a,t)$*

The dependent variables of the motion are $z(a,t)$ and $\Gamma(a,t)$. To obtain equations for these quantities two conditions, one kinematic and the other dynamic, must be satisfied on C. The kinematic condition is the usual requirement that the two contiguous surfaces bounding the fluid 1 and fluid 2, which meet at and define C, should each always consist of the same material particles, thus allowing local relative tangential motion of these surfaces at C, but not local relative normal motion. An equation for $z(a,t)$ that automatically satisfies the kinematic condition may be formulated by extending the now standard convention of defining the velocity $\dot{z} = (\partial z/\partial t)_a = u + iv$ of a marker particle on C as

$$\dot{z}^* = \left(\frac{dW}{dz}\right)_{\mathrm{p}} + \tfrac{1}{2}f(a)\frac{\partial\Gamma}{\partial a}\left(\frac{\partial z}{\partial a}\right)^{-1}, \tag{9}$$

where

$$\left(\frac{dW}{dz}\right)_{\mathrm{p}} = \frac{1}{2\pi i}\oint_{-\frac{1}{2}\pi}^{\frac{1}{2}\pi} \cot[z(a,t) - z(a',t)]\frac{\partial\Gamma'}{\partial a'}da' + \bar{U}, \tag{10}$$

and where z^* is the complex conjugate of z. The integral in (10) is a CPV integral, being the mean of the generally unequal values obtained as $Z \to z(a,t)$ on C from either side. In (9) we have defined our marker-particle velocity as the weighted average of the complex velocities on either side of C, the weights being chosen as $\frac{1}{2}[1+f(a)]$ and $\frac{1}{2}[1-f(a)]$ for the fluid 1 and fluid 2 sides respectively. The function $f(a)$ is an observer-

chosen, continuous single-valued function which satisfies (at least) $1 \geqslant f \geqslant -1$ for $\frac{1}{2}\pi \geqslant a \geqslant -\frac{1}{2}\pi$. The role of $f(a)$ in the present formulation of the interface motion is discussed further in appendix A.

The dynamic condition to be satisfied is that the pressure difference between the fluids at C must be balanced by the interfacial force due to surface tension. If we denote these pressures by p_1 and p_2, this requirement may be written in dimensionless form as

$$p_1 - p_2 = -\frac{1}{2}\left|\frac{\rho_1-\rho_2}{\rho_1+\rho_2}\right| \beta^2 \kappa. \tag{11}$$

In (11)

$$\kappa(a,t) = \frac{\mathscr{I}\{\partial z^*/\partial a\, \partial^2 z/\partial a^2\}}{|\partial z/\partial a|^3}, \tag{12}$$

$$\beta = \frac{\lambda_c}{\lambda}, \tag{13}$$

where κ is the curvature of C, $\mathscr{I}$ denotes the imaginary part of a complex argument and $\lambda_c = 2\pi\{g/\gamma|\tilde{\rho}_1 - \tilde{\rho}_2|\}^{-\frac{1}{2}}$ is a critical wavelength (see §4.1), γ being the interfacial-tension coefficient for the fluid pair.

To express (11) in terms of (z, Γ) we now write Bernoulli's equation in the fluids 1 and 2 respectively as

$$p_1(Z,t) = -\rho_1\left[\left(\frac{\partial\phi}{\partial t}\right)_1 + \frac{1}{2}\left|\frac{dW}{dZ}\right|_1^2 + Y\right] + P_1(t), \tag{14}$$

$$p_2(Z,t) = -\rho_2\left[\left(\frac{\partial\phi}{\partial t}\right)_2 + \frac{1}{2}\left|\frac{dW}{dZ}\right|_2^2 + Y\right] + P_2(t), \tag{15}$$

where $P_1(t)$ and $P_2(t)$ are arbitrary functions of time, and $(\partial\phi/\partial t)_1$ and $(\partial\phi/\partial t)_2$ are understood to be derivatives at fixed Z. We now let $Z \to z(a,t)$ from each side of C in (14) and (15), and substitute the difference between these equations into (11), using (2) to express ρ_1 and ρ_2 in terms of α. The discontinuity in $\partial\phi/\partial t$ across C may be evaluated by taking $(\partial/\partial t)_Z$ of (5) and integrating by parts the $\log[\sin(Z-z')]$ integral in the result. The $|dW/dZ|^2$ terms can be treated through (6) and (9). After some lengthy algebra, we finally obtain

$$\dot{\Gamma} + \frac{\alpha}{\pi}\int_{-\frac{1}{2}\pi}^{\frac{1}{2}\pi} \dot{\Gamma}'\, \mathscr{I}\left[\frac{\partial z'}{\partial a'}\cot(z-z')\right] da' = Q(a,t) + 2[P_1(t) - P_2(t)] + S(t), \tag{16}$$

where

$$Q(a,t) = \alpha\left\{\frac{1}{\pi}\fint_{-\frac{1}{2}\pi}^{\frac{1}{2}\pi} \frac{\partial\Gamma'}{\partial a'}\mathscr{I}[\dot{z}'\cot(z-z')]\, da' - \left|\left(\frac{dW}{dz}\right)_p\right|^2 - 2y\right\}$$

$$+ \tfrac{1}{2}(f - \tfrac{1}{2}\alpha)\left(\frac{\partial\Gamma}{\partial a}\right)^2\left|\frac{\partial z}{\partial a}\right|^{-2} + \tfrac{1}{2}|\alpha|\beta^2\kappa(a,t) \tag{17}$$

and $\dot{\Gamma} = (\partial\Gamma/\partial t)_a$. In (17), $\dot{z}$ and $(dW/dz)_p$ are given by (9) and (10), while $S(t)$ is a known function of time which arises from the $\partial\phi/\partial t$ discontinuity across C. Together with $P_1(t)$ and $P_2(t)$, $S(t)$ may be eliminated by noting that by definition we must have

$$\dot{\Gamma}(\tfrac{1}{2}\pi, t) = \dot{\Gamma}(-\tfrac{1}{2}\pi, t) = 0.$$

Putting $a = \frac{1}{2}\pi$ in (16) and (17), and subtracting the result from (16) then leads to a set of initial-value equations for $z(a,t)$ and for $\Gamma(a,t)$ as

$$\dot{z}^* = \left(\frac{dW}{dz}\right)_p + \tfrac{1}{2}f\frac{\partial\Gamma}{\partial a}\left(\frac{\partial z}{\partial a}\right)^{-1}, \tag{18}$$

$$\dot{\Gamma} + \frac{\alpha}{\pi}\int_{-\frac{1}{2}\pi}^{\frac{1}{2}\pi} \dot{\Gamma}'\,\mathscr{I}\left\{\frac{\partial z'}{\partial a'}[\cot(z-z') - \cot(z_N - z')]\right\} da' = Q(a,t) - Q(\tfrac{1}{2}\pi, t), \tag{19}$$

where $z_N = z(\frac{1}{2}\pi, t)$.

Equation (19) expresses the rate of change of circulation following marker particles due to the action of gravity, differential tangential accelerations of either side of C, surface tension and our choice of weighting function. For known $z(a,t)$ and $\Gamma(a,t)$, $\dot{z}(a,t)$ follows from (18). The right-hand side of (19) may then be evaluated, but this equation as a whole is a Fredholm integral equation of the second kind for $\dot{\Gamma}(a,t)$ which must be solved in order to integrate forward in time. For given α, β, F and $f(a)$, (18) and (19) together with (12) and (17) and specified initial conditions $[z(a,0), \Gamma(a,0)]$ are the basis of the present calculations. Birkhoff's (1962) formulation of the interfacial motion may be obtained by putting $F = \beta = 0, f(a) = 0$ and by differentiating (19) with respect to a. Note that, for $\alpha = 0, f(a) = 0$, (19) then shows that $\Gamma(a,t) = \Gamma(a,0)$, while (18) reduces to the usual equation for the motion of a periodic vortex sheet. In this case the stabilizing effect of surface tension at infinitesimal wavelengths is absent.

2.3. *Integral invariants of the motion*

There exist several integral properties of the flow which should remain invariant with time whatever the motion of C, and which can be monitored in a computational solution of (18) and (19) as a check on its accuracy. Considerations of overall mass conservation show that Ω, the mass flux across C per wavelength, and $\bar{y}$, the mean level of C, should remain invariant. These quantities are given by

$$\Omega = -\int_{-\frac{1}{2}\pi}^{\frac{1}{2}\pi} \mathscr{I}\left[\dot{z}^*\left(\frac{\partial z}{\partial a}\right)\right] da, \tag{20}$$

$$\bar{y} = \frac{1}{\pi}\int_{-\frac{1}{2}\pi}^{\frac{1}{2}\pi} y\left(\frac{\partial x}{\partial a}\right) da. \tag{21}$$

In our chosen reference framework the X-momentum L_x per wavelength (see appendix B) should also be invariant, since gravity acts only in the y-direction. The energy of the motion has three components, namely the potential energy, the interfacial surface energy associated with work done against surface tension in deforming C and the kinetic energy. Taking $y(a,t) = 0$ as the datum for potential and interfacial surface energy, the first two of these quantities are given respectively by

$$V(t) = -\alpha\int_{-\frac{1}{2}\pi}^{\frac{1}{2}\pi} y^2\frac{\partial x}{\partial a} da, \tag{22}$$

$$U_s(t) = \frac{|\alpha|\beta^2}{2}\left[\int_{-\frac{1}{2}\pi}^{\frac{1}{2}\pi}\left|\frac{\partial z}{\partial a}\right| da - \pi\right]. \tag{23}$$

For $F \neq 0$, or $\alpha < 1$, the kinetic energy is infinite owing to finite fluid velocities at $Y \to \pm\infty$. In appendix B we give arguments to show that $T(t)$ given by (53) is the

appropriate finite quantity associated with the two-fluid kinetic energy per wavelength. Hence we may expect that

$$E = V(t) + U_s(t) + T(t), \tag{24}$$

is an invariant of the motion associated with the total energy per wavelength. Equation (24) may be shown to yield the correct total energy per wavelength for the case $F = 0$, $\alpha \neq 0$, and also for $\alpha = 1$, $F \neq 0$.

3. Numerical method of solution

We shall replace (18) and (19) by a finite number of ordinary differential equations. The interval $\frac{1}{2}\pi \geqslant a \geqslant -\frac{1}{2}\pi$ is thus divided into $N-1$ equal sub-intervals of length $\Delta a = \pi/(N-1)$, the end points of which we denote by a_k $(k = 1, \ldots, N)$, with $a_1 = -\frac{1}{2}\pi$ and $a_N = \frac{1}{2}\pi$. These a_k then label N marker particles on C. At time t we denote the positions and circulations of these particles by $z_k(t) = x_k(t) + iy_k(t) = z(a_k, t)$ and $\Gamma_k(t) = \Gamma(a_k, t)$ $(k = 1, \ldots, N)$ respectively, while the instantaneous time derivatives of these quantities are denoted by $\dot{z}_k$ and $\dot{\Gamma}_k$ $(k = 1, \ldots, N)$. Since $z_N = z_1 + \pi$ and since Γ_1 and Γ_N are constants, we are then left with $3N-4$ dependent variables for which we shall obtain first-order ordinary differential equations in time of the form

$$\left.\begin{aligned} \dot{z}_k(t) &= \dot{z}_k[\Theta] \quad (k = 1, \ldots, N-1), \\ \dot{\Gamma}_k(t) &= \dot{\Gamma}_k[\Theta] \quad (k = 2, \ldots, N-1), \end{aligned}\right\} \tag{25}$$

where $\Theta = (\alpha, \beta, F; N; a_1, \ldots, a_N; z_1, \ldots, z_N; \Gamma_1, \ldots, \Gamma_N)$ represents a complete set of parameters defining the instantaneous state of motion.

For given Θ, the right sides of (25) are to be calculated through a numerical approximation to (18) and (19), evaluated at a_k $(k = 1, \ldots, N)$.

This requires (i) finite-difference estimates of $\partial/\partial a$ derivatives; (ii) the replacement of the CPV integrals in (17) and (10) by numerical integration formulae; (iii) the solution of the integral equation (19) for $\dot{\Gamma}(a, t)$; (iv) a method of integrating (25) forward in time.

The derivatives required are $(\partial z/\partial a)_k$, $(\partial^2 z/\partial a^2)_k$, $(\partial \Gamma/\partial a)_k$, $(\partial^2 \Gamma/\partial a^2)_k$ and $(\partial \dot{z}/\partial a)_k$, where $(\partial/\partial a)_k$ refers to a derivative evaluated at a_k. The $(\partial z/\partial a)_k$ and $(\partial \Gamma/\partial a)_k$ were evaluated by applying periodic cubic splines for equal intervals (see Ahlberg, Nilson & Walsh 1967, chap. 2) to the periodic functions defined by (8). The second derivatives were then obtained by a spline-on-spline technique from the known first derivatives. The $(\partial \dot{z}/\partial a)_k$ were also evaluated by periodic splines applied to the previously calculated $\dot{z}_k$ $(k = 1, \ldots, N)$.

3.1. *Treatment of the singular integrals and solution of the integral equation*

The CPV integrals in (10) and (17) may both be regarded as special cases of the general integral

$$I(a) = \fint_{-\frac{1}{2}\pi}^{\frac{1}{2}\pi} g(a') \cot [z(a) - z(a')]\, da', \tag{26}$$

where $g(a)$ is a known, complex, periodic function of a. This integral was evaluated by first writing it as

$$I(a) = \int_{-\frac{1}{2}\pi}^{\frac{1}{2}\pi} g(a')K(a,a')\,da' - \left(\frac{\partial z}{\partial a}\right)^{-1} \int_{-\frac{1}{2}\pi}^{\frac{1}{2}\pi} J(a,a')\,da' + g(a)\left(\frac{\partial z}{\partial a}\right)^{-1} \oint_{-\frac{1}{2}\pi}^{\frac{1}{2}\pi} \cot(a-a')\,da', \tag{27}$$

where

$$\left.\begin{aligned} K(a,a') &= \cot[z(a)-z(a')] - \left(\frac{\partial z}{\partial a}\right)^{-1} \cot(a-a'), \\ J(a,a') &= [g(a)-g(a')]\cot(a-a'). \end{aligned}\right\} \tag{28}$$

In (27) the singularity has been isolated into the third integral, which may be shown to vanish identically. The first two integrands are bounded and analytic at $a = a'$, with $K(a,a) = \frac{1}{2}(\partial^2 z/\partial a^2)/(\partial z/\partial a)^2$ and $J(a,a) = \partial g/\partial a$. The corresponding integrals were calculated numerically using a 4-point Lagrangian formula (see Abramowitz & Stegun 1972, p. 215) to evaluate contributions over each Δa, leading to

$$I_k = \sum_{j=1}^{N} w_j g(a_j) K(a_k, a_j) - \left(\frac{\partial z}{\partial a}\right)_k^{-1} \sum_{j=1}^{N} w_j J(a_k, a_j), \tag{29}$$

where $I_k = I(a_k)$, and $w_j (j = 1, \ldots, N)$ are known integration weights. The term for $j = k$ in the first sum of (29) leads to the curvature correction discussed by van de Vooren (1980), Baker (1980) and Moore (1980). Since $g(a) = \partial\Gamma/\partial a$ and $\dot{z}(\partial\Gamma/\partial a)$ respectively for the integrals in (10) and (17), the $j = k$ term in the second sum yields the previously noted derivatives $\partial^2\Gamma/\partial a^2$ and $\partial\dot{z}/\partial a$.

A numerical solution of the integral equation (19) was obtained by first writing it in the convenient form

$$\dot{\Gamma} + \frac{\alpha}{\pi}\int_{-\frac{1}{2}\pi}^{\frac{1}{2}\pi} (\dot{\Gamma}' - \dot{\Gamma})\mathscr{I}\left[\left(\frac{\partial z'}{\partial a'}\right)\cot(z-z')\right]da' - \frac{\alpha}{\pi}\int_{-\frac{1}{2}\pi}^{\frac{1}{2}\pi} \dot{\Gamma}'\mathscr{I}\left[\left(\frac{\partial z'}{\partial a'}\right)\cot(z_N - z')\right]da' = Q(a,t) - Q(\tfrac{1}{2}\pi, t), \tag{30}$$

which is valid by virtue of $\oint_C \cot(z-z')\,dz' \equiv 0$. The integrand of the first integral on the left now vanishes at $a = a'$. The integrals were each split into $N-1$ integrals over each Δa, which were then approximated using the 4-point Lagrangian integration formula. For given Θ, evaluating (30) thus at $a_k (k = 2, \ldots, N)$ gives a set of $N-2$ linear equations for the $\dot{\Gamma}_k$ $(k = 2, \ldots, N)$ with known coefficients, which were solved by a standard method.

3.2. *Solution of the ordinary differential equations*

Equations (25) were integrated forward in time using the IMSL (1978) FORTRAN IV differential equation solver DGEAR. Of several options available in DGEAR, a self-starting Adams–Bashforth predictor–corrector method for non-stiff equations was chosen. This method automatically varies the order of the predictor–corrector and chooses the current time step Δt such that the single-step error does not exceed a user-specified error per time step in the root-mean-square norm. The method is well-

documented (see Gear 1971), and has been previously utilized by the author for the solution of related interfacial motion problems (see Pullin 1981).

The number of evaluations of $(\dot{z}_k, \dot{\Gamma}_k)$ required per Δt by DGEAR varies with the current order of the predictor–corrector. In the present application the complete scheme for the calculation of the $(\dot{z}_k, \dot{\Gamma}_k)$ was implemented for each evaluation including solution of the integral equation. With $N = 91$ points along C about 4·1 s of the University of Melbourne CDC CYBER-72 computer central processing time was required for each calculation of the 269 time derivatives. The major portion of this time (about 75 %) was used to compute the cot $(z_k - z_j)$, while about 20 % was used for solution of (30). At each Δt the invariants $\Omega, \bar{y}, L_x$ and E were calculated, the last two of which require knowledge of $W_k = W(a_k, t)\,(k = 1, \ldots, N)$ on C in addition to the current (z_k, Γ_k) set. These were obtained through evaluation of the right side of (5) after suitable rearrangement of the integral and integration by parts.

3.3. *Tests on interfacial and free-surface waves*

The numerical method was tested by calculating the motion of a nonlinear progressive interfacial wave from known initial conditions obtained from the solutions of Holyer (1979). A wave with a value of Holyer's amplitude parameter of 0·1 was chosen with $\alpha = 0{\cdot}8182$ $(\rho_2/\rho_1 = 0{\cdot}1)$ and $F = 0$. This is a slightly nonlinear gravity wave (no surface tension) with crest height of 0·052061 and depth of 0·047940 moving with velocity of 0·642269. The equivalent linearized wave velocity is 0·639602. A value of $N = 51$ points on C was chosen while values of (z_k, Γ_k) kindly supplied by Dr Holyer were used as initial conditions. It was found however that, after about 1–1·5 wave periods, a saw-rooth-like instability appeared in the y- and Γ-profiles, similar to that encountered by Longuet-Higgins & Cokelet (1976) in the equivalent test of their free-surface-wave technique. This instability also occurred in other flows treated here, generally growing rather more rapidly in cases involving finite surface-tension terms. The instability seems unlikely to be physical in nature since it appeared in known stable configurations always on the scale of Δa. Its ultimate cause remains unknown.

Longuet-Higgins & Cokelet removed the instability by applying 5-point smoothing to their dependent variables every 10 time steps. Here a different scheme was adopted. Five-point smoothing was applied to the (z_k, Γ_k) set at every time step, but only for the purposes of evaluating the $(\dot{z}_k, \dot{\Gamma}_k)$ set through (18) and (19), so that the smoothed values themselves were not fed back into the time-stepping routine. In addition $(\partial/\partial a)_k$ arrays were 5-point smoothed before applying the spline-on-spline technique to evaluate $(\partial^2/\partial a^2)_k$ arrays. This procedure appeared to eliminate the saw-tooth instability with little direct effect on the independent variables and the integral invariants. Using this scheme for the progressive wave flow, the computed wave-crest height and depth after about two wave periods were 0·051 96 and 0·048 02 respectively, while the calculated wave speed was 0·6425. The kinetic and potential energies remained constant to $O(10^{-6})$ and agree with Holyer's computed values to $O(10^{-5})$.

A test was also carried out on a free-surface breaking wave. Unlike Longuet-Higgins & Cokelet (1976), who forced their nonlinear progressive waves to break by application of a varying surface pressure field, here we chose initial conditions corresponding to an initially finite-amplitude sinusoidal wave of energy larger than that of the highest free-surface wave. Breaking then occurs at constant surface pressure. The result with $F = 0, \alpha = 1, \beta = 0, f = 1$ and amplitude $\epsilon = \frac{1}{10}\pi$ is shown in figure 1, which depicts a

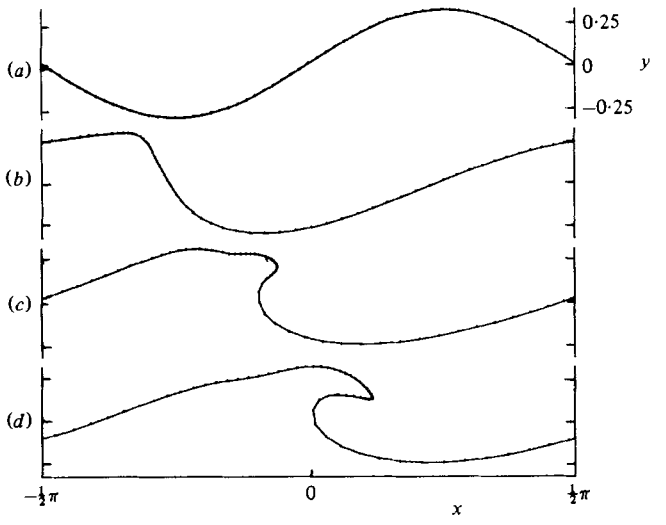

FIGURE 1. Time sequence of profiles for constant-pressure breaking wave, $\alpha = 1$, $F = 0$, $\beta = 0$, initial amplitude $= \frac{1}{10}\pi$: (*a*) $t = 0$, (*b*) 1·0, (*c*) 1·75, (*d*) 2·25.

sequence of plots of the wave shape for $t \geqslant 0$. The wave may be seen to form a region of high curvature near the crest, followed by smooth breaking. At $t = 0$ in figure 1(*a*) $\tilde{y} = 3{\cdot}2 \times 10^{-7}$, $\Omega = 1{\cdot}7 \times 10^{-7}$, $L_x = 0{\cdot}069805$ and $E = 0{\cdot}323487$, while at $t = 2{\cdot}25$ in figure 1(*d*) the values $\tilde{y} = 2{\cdot}1 \times 10^{-5}$, $\Omega = 4{\cdot}7 \times 10^{-4}$, $L_x = 0{\cdot}069625$ and $E = 0{\cdot}323396$ were calculated, with similar values for intermediate times.

4. Kelvin–Helmholtz instability

4.1. *Linearized theory*

For $\tilde{\rho}_1 > \tilde{\rho}_2$, the two-fluid interface may be subject to Kelvin–Helmholtz instability for sufficiently large $|\tilde{U}_1 - \tilde{U}_2|$. In terms of dimensional co-ordinates, it may be shown (e.g. Yih 1969, chap. 8) that the evolution of small disturbances to C proportional to $\exp[ik\tilde{x} - \omega\tilde{t}]$ follows a dispersion relation of the form

$$\omega^2 = \frac{k^2(\tilde{U}_1 - \tilde{U}_2)^2\tilde{\rho}_1\tilde{\rho}_2}{(\tilde{\rho}_1 + \tilde{\rho}_2)^2} - \left[gk\left(\frac{\tilde{\rho}_1 - \tilde{\rho}_2}{\tilde{\rho}_1 + \tilde{\rho}_2}\right) + \frac{\gamma k^3}{\tilde{\rho}_1 + \tilde{\rho}_2}\right], \tag{31}$$

where $k = 2\pi/\lambda$ is the disturbance wavenumber. Analysis of (31) further shows that the interface motion is stable at all λ provided that $\Delta\tilde{U} = |\tilde{U}_1 - \tilde{U}_2| < \Delta\tilde{U}_c$, where

$$\Delta\tilde{U}_c^2 = 2\left(\frac{\tilde{\rho}_1 + \tilde{\rho}_2}{\tilde{\rho}_1\tilde{\rho}_2}\right)[\gamma g(\tilde{\rho}_1 - \tilde{\rho}_2)]^{\frac{1}{2}}. \tag{32}$$

The onset of instability first occurs for $\Delta\tilde{U} = \Delta\tilde{U}_c$ and at a critical wavelength given by

$$\lambda_c = 2\pi\left\{\frac{g}{\gamma}(\tilde{\rho}_1 - \tilde{\rho}_2)\right\}^{-\frac{1}{2}}. \tag{33}$$

For $\Delta\tilde{U} > \Delta\tilde{U}_c$ the flow is unstable for all $\lambda > \lambda_s$, where

$$\lambda_s = \lambda_c[K + (K^2 - 1)^{\frac{1}{2}}]^{-1}. \tag{34}$$

The maximum growth rate occurs at

$$\lambda_m = 1{\cdot}5\lambda_c[K + (K^2 - 0{\cdot}75)^{\frac{1}{2}}]^{-1}, \tag{35}$$

α	β	F	S	δ_s	ϵ/π	N
0·125	1·0	−0·25	−0·077	—	0·01	45*
0·125	0·0	−0·75	0·372	0·0	0·01	91
0·125	1·0	−0·75	0·310	0·461	0·005	45
0·125	1·0	−0·75	0·310	0·461	0·01	91
0·125	1·0	−0·75	0·310	0·461	0·0333	91
0·125	1·0	−0·75	0·310	0·461	0·10	91
0·750	1·0	−2·0	0·999	0·933	0·005	45
0·750	1·0	−2·0	0·999	0·933	0·01	91
0·750	1·0	−2·0	0·999	0·933	0·0333	91

TABLE 1. Values of parameters for Kelvin–Helmholtz instability; * indicates linearized stability

where

$$K = (\Delta\bar{U}/\Delta\bar{U}_c)^2 = \pi(1-\alpha^2)\,F^2(4|\alpha|\beta)^{-1}. \tag{36}$$

We shall study the evolution of disturbances to the shape of C given at $t = 0$ by $y = -\epsilon \sin 2x$, where ϵ is the amplitude. We choose $\Gamma(x, 0)$ corresponding to the normal-mode solutions. If we define

$$S = \omega^2\lambda/4\pi g = \tfrac{1}{4}[(1-\alpha^2)\,F^2 - 2(\beta^2|\alpha| + \alpha)], \tag{37}$$

then the normal-mode linearized solutions may be expressed in the form

$$\left.\begin{aligned} y &= -\epsilon e^{2c_i t}\sin[2(x-c_r t)], \\ \Gamma &= \pi^{\frac{1}{2}}F(x-\tfrac{1}{2}\pi) + 2\epsilon e^{2c_i t}\{(c_r+\bar{U})\cos[2(x-c_r t)] - c_i \sin[2(x-c_r t)]\}. \end{aligned}\right\} \tag{38}$$

In (38) for $S < 0$ (stable), $c_r = (-S)^{\frac{1}{2}}$, $c_i = 0$. The solution is a stable wave propagating with period $T_w = \pi c_r^{-1}$. For $S > 0$ (unstable), $c_r = 0$, $c_i = S^{\frac{1}{2}}$. Here the disturbance grows exponentially with e-folding time $T_e = (2c_i)^{-1}$. Equations (32) and (33) show that instability will first occur at $\beta = 1$ and at a critical Froude number

$$F = \left[\frac{4\alpha}{\pi(1-\alpha^2)}\right]^{\frac{1}{2}}. \tag{39}$$

4.2. *Present results*

The initial conditions were defined by $x_k = -\frac{1}{2}\pi + (k-1)\,\Delta a$ $(k = 1, \ldots, N)$, where $\Delta a = \pi/(N-1)$, with $y(x_k, 0)$ and $\Gamma(x_k, 0)$ being calculated from (38). Table 1 summarizes the parameters of the cases discussed presently. For most cases $\beta = 1{\cdot}0$ was used since this is the critical value suggested by linear theory and which is also supported by the experimental evidence of Thorpe (1969). The value $\alpha = 0{\cdot}125$ was chosen since it corresponds to that used in some of Thorpe's experiments, but other values are arbitrary. Negative values of F were used to obtain a conventional clockwise roll-up tendency, while the value of the velocity-weighting function was chosen as $f(a) = \text{const.} = \alpha$ for all cases. For adequate resolution along C it is clearly desirable that $\delta_s = \pi\lambda_s/\lambda \gg \Delta a$. For given N, (34)–(36) show that this condition places practical limitations on the values of β and F that can be used, so that for example flows in which capillary effects are reduced ($\beta \ll 1$), or those strongly dominated by inertial forces ($\beta = 1$, $F \gg 1$), cannot be treated realistically. Thus, we have generally chosen $F \sim O(1)$, in which case buoyancy, inertial and surface-tension forces are all of the

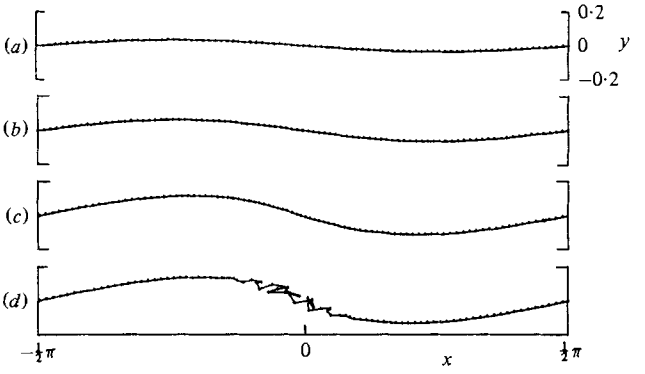

FIGURE 2. Time sequence of profiles for two-fluid interface, $\alpha = 0{\cdot}125$, $F = -0{\cdot}75$, $\beta = 0$, $\epsilon = \frac{1}{100}\pi$: (*a*) $t_1 = 0$, (*b*) 0·6218, (*c*) 1·2093, (*d*) 1·4009.

same order. An estimate of the minimum allowable Δt follows by supposing that the smallest resolvable length scale is the local arc-length increment $\Delta s \sim O(\pi/N)$. If waves of length Δs are stabilized by surface tension, it follows from (31) that the dimensionless time scale (period) associated with their linearized normal modes is

$$\Delta T = \{2/\pi\alpha\beta^2\}^{\frac{1}{2}} \Delta s^{\frac{3}{2}}. \tag{40}$$

Resolution of this motion requires that $\Delta t \ll \min(\Delta T)$. Checks were carried out during the simulations described here and in § 5 to ensure that this condition was not violated.

For the stable flow case listed in table 1 the wave speed was estimated by following the maximum in the wave profile over somewhat less than two wave periods. The value obtained was 0·295, compared with the linearized value of 0·277, thus indicating that nonlinear effects may be substantial even for ϵ/λ of order 10^{-2}. Zalosh (1976) also found differences between finite-amplitude calculations and linear theory, but the discrepancy was of opposite sign. The values of the calculated integral invariants for the stable case were as follows: both $\bar{y}$ and Ω were $O(10^{-7})$ throughout the first wave period, increasing to $O(10^{-5})$ towards the end of the second. The change in X-momentum $\Delta L_x = L_x(t) - L_x(0)$ showed similar variation, while $\Delta E = E(t) - E(0)$ was $O(10^{-5})$ at the end of the first period and $O(10^{-4})$ towards the end of the second. It was noted that the wave amplitude increased by about 30 % during the run, indicating a possible long-time-scale instability associated with finite amplitude.

Figure 2 shows the evolution of the interface for the unstable case of table 1 with $\beta = 0$ chosen to simulate zero surface tension. Note that time is specified as $t_1 = 2S^{\frac{1}{2}}t$ as suggested by (38). The interface shape is smooth at $t_1 = 1{\cdot}2093$ (figure 2*c*) but has developed severe irregularities at $t = 1{\cdot}4009$ (figure 2*d*) before there is any suggestion of large-scale roll-up-like behaviour. For this case it is easy to show that $\delta_8 = 0$. Hence the most likely cause of this behaviour is discrete Helmholtz instability on the scale of Δs as a numerical consequence of the short-wave-instability problem.

The inclusion of surface tension in the case depicted in figure 3 with $\beta = 1{\cdot}0$ leads to more-coherent behaviour. The crest–trough amplitude grows uniformly at first, as predicted by the linear theory. Here $\delta = 0{\cdot}461 \gg \Delta a = 0{\cdot}0349$, so that the resolution is at least initially adequate in the linear regime. By $t_1 = 1{\cdot}6005$ one of the points of inflection on the profile in figure 3 has developed into a region of rapidly increasing slope as nonlinear effects become evident. At $t_1 = 1{\cdot}6526$ this part of the interface

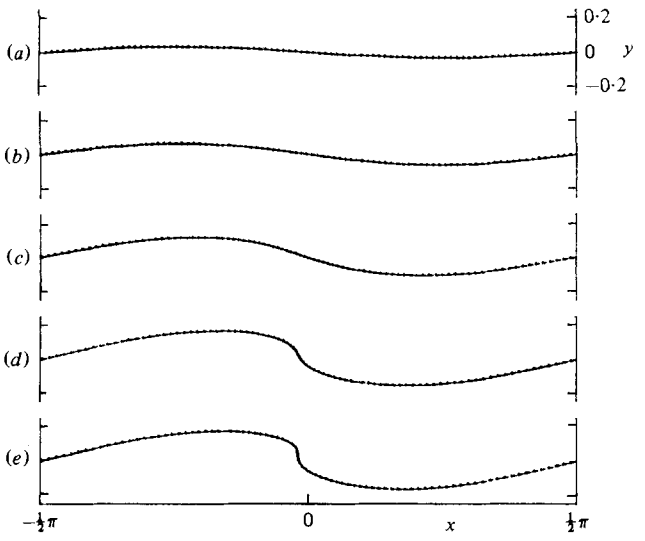

FIGURE 3. Time sequence of profiles for two-fluid interface, $\alpha = 0{\cdot}125$, $F = -0{\cdot}75$, $\beta = 1{\cdot}0$, $\epsilon = \frac{1}{100}\pi$: (*a*) $t_1 = 0$, (*b*) 0·6218, (*c*) 1·2102, (*d*) 1·6005, (*e*) 1·6526.

becomes vertical as the wave is about to break. For greater values of t_1 the interface did not roll up smoothly but rather developed small irregularities on the vertical section. These are shown in detail in figure 4(*a*), which depicts a sequence of close-up plots of the interface profile in the near-vertical region, spaced at equal time intervals. Figure 5 shows the evolution of the interface in an unstable configuration with $\alpha = 0{\cdot}75$. The profile develops a sharp crest, which was found to be characteristic of near-unity values of α. This flow also led to the appearance of small-scale corrugations, which may be seen to the right of the profile crest in figure 5(*e*) and more clearly in the close-up sequences of figure 6. The eventual development of these fine-scale motions occurred in all of the flows in which surface tension was included, usually beginning in high-curvature sections of the profile. Possible interpretations of this behaviour are discussed subsequently.

It is convenient here to give values of the integral invariants of the calculation of figure 3. By $t_1 = 1{\cdot}2102$ (frame *c*) $\bar{y}$, Ω and ΔL_x were all $O(10^{-8})$, with $\Delta E \sim O(10^{-5})$. At $t_1 = 1{\cdot}6526$ (frame *e*) $\bar{y}$ had increased to $O(10^{-6})$, Ω to $O(10^{-4})$, ΔL_x to $O(10^{-6})$, while ΔE remained $O(10^{-5})$. The potential, kinetic and surface energies at this point were respectively $O(10^{-3})$, $O(10^{-2})$ and $O(10^{-2})$. These values were typical of other calculations reported here.

Several simulations with $N = 45$ were carried out to determine the effect of ϵ on the broad features of the primary instability. Generally, there was found to be excellent agreement with the linear theory up to the time at which the interface developed a very steep section with a subsequent underprediction of the maximum Y-displacement. The effect of ϵ on the profile shape at the value of t for which the profile first developed a nearly vertical section was also investigated as a measure of the influence of a finite initial perturbation on the nonlinear growth of the unstable normal modes. The values of ϵ/π so tested are shown in table 1. The results indicated that for the two cases $(\alpha, \beta, F) = (0{\cdot}125, 1{\cdot}0, -0{\cdot}75)$ and $(0{\cdot}75, 1{\cdot}0, -2{\cdot}0)$, the effect of amplitude becomes small for $\epsilon/\pi < 10^{-2}$.

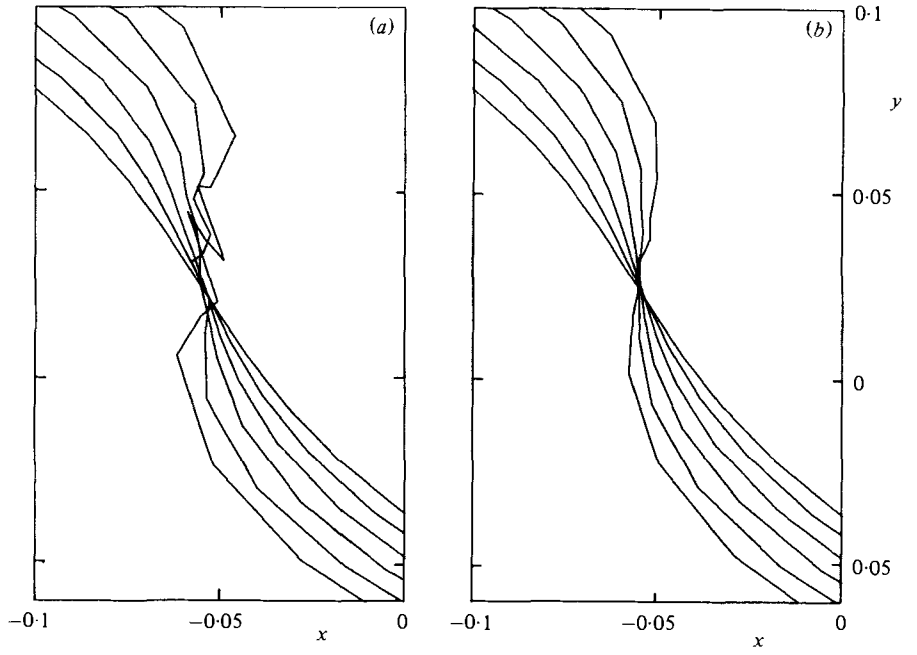

FIGURE 4. Close-up of interface profile at equal time intervals, $\alpha = 0{\cdot}125$, $F = -0{\cdot}75$, $\beta = 1{\cdot}0$, $\epsilon = \frac{1}{100}\pi$, $1{\cdot}6904 \geqslant t_1 \geqslant 1{\cdot}5867$: (*a*) smoothing for time derivatives only; (*b*) smoothing of dependent variables.

5. Rayleigh–Taylor instability

5.1. *Linearized theory*

Pure Rayleigh-Taylor instability may be generated by putting $F = 0$ with $\alpha < 0$. For initial conditions given by $y(x, 0) = -\epsilon \cos 2x$, $\Gamma(x, 0) = 0$, the linearized normal-mode solution may be written as

$$\left.\begin{aligned} y(x,t) &= -\epsilon \cosh \omega t \cos 2x, \\ \Gamma(x,t) &= -\omega\epsilon \sinh \omega t[\cos 2x + 1], \end{aligned}\right\} \tag{41}$$

where $\omega^2 = 2|\alpha|(1-\beta^2)$. It follows that for $\beta > 1$ ($\lambda < \lambda_c$) the interface is stabilized by interfacial tension, undergoing oscillations of period $T_w = 2\pi[2|\alpha|(\beta^2-1)]^{-\frac{1}{2}}$. For $\beta < 1$ unstable exponential growth of interfacial shape perturbations results. By returning to physical co-ordinates, it may be easily verified that the maximum growth rate of a single mode disturbance occurs at a wavelength corresponding to a value of $\beta = \sqrt{\frac{1}{3}} = 0{\cdot}5774$.

5.2. *Present results*

Owing to the geometrical symmetry of the interface profile about $X = 0$ it is sufficient to follow the motion of a half-wavelength in $\frac{1}{2}\pi \geqslant a \geqslant 0$, with resulting savings in computational effort. The calculations were carried out with $N = 61$ points on the half-wavelength. Values of $\alpha = -0{\cdot}998$, $-0{\cdot}5$ and $-0{\cdot}0637$ were chosen, the first and last of which correspond approximately to the air–water and benzene–water combinations studied experimentally by Lewis (1950). The initial conditions were defined by

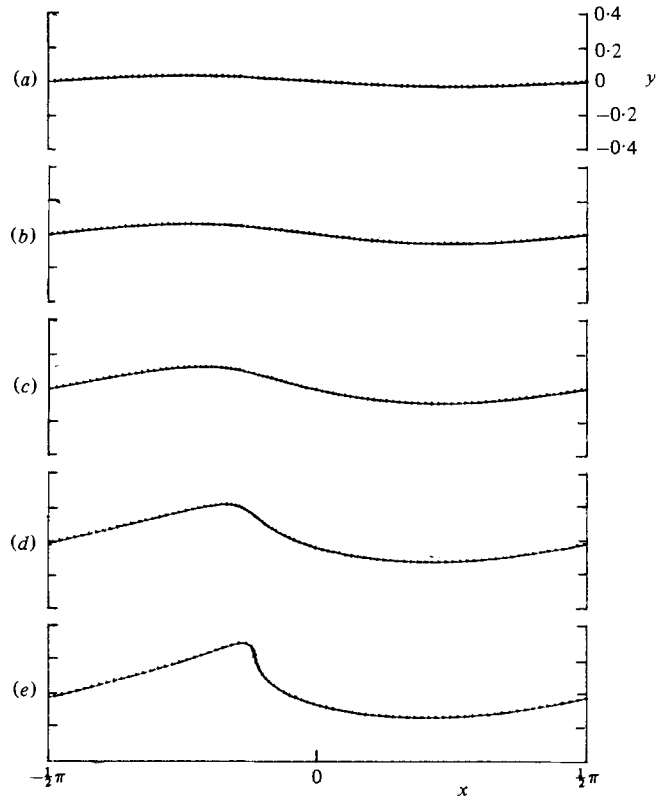

FIGURE 5. Time sequence of profiles for two-fluid interface, $\alpha = 0{\cdot}75$, $F = -2{\cdot}00$, $\beta = 1{\cdot}0$, $\epsilon = \frac{1}{100}\pi$: (*a*) $t_1 = 0$, (*b*) 0·6149, (*c*) 1·2150, (*d*) 1·6050, (*e*) 1·7854.

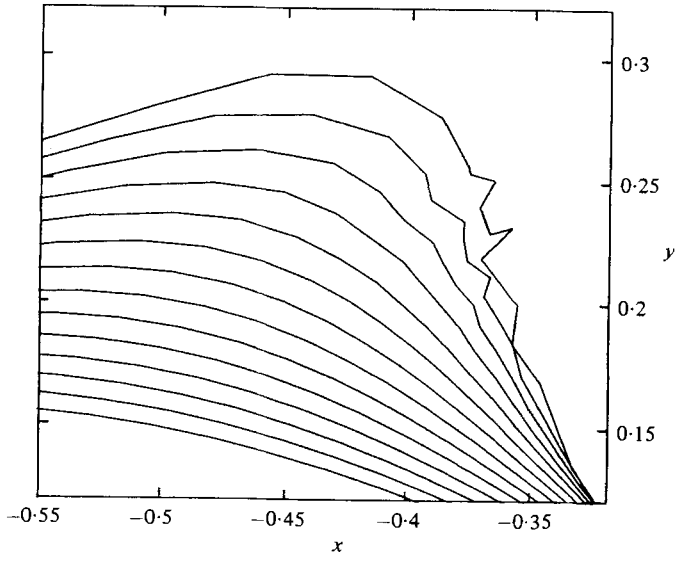

FIGURE 6. Close-up of interface profiles at equal time intervals, $\alpha = 0{\cdot}75$, $F = -2{\cdot}0$, $\beta = 1$, $\epsilon = \frac{1}{100}\pi$, $1{\cdot}7859 \geqslant t_1 \geqslant 1{\cdot}4285$.

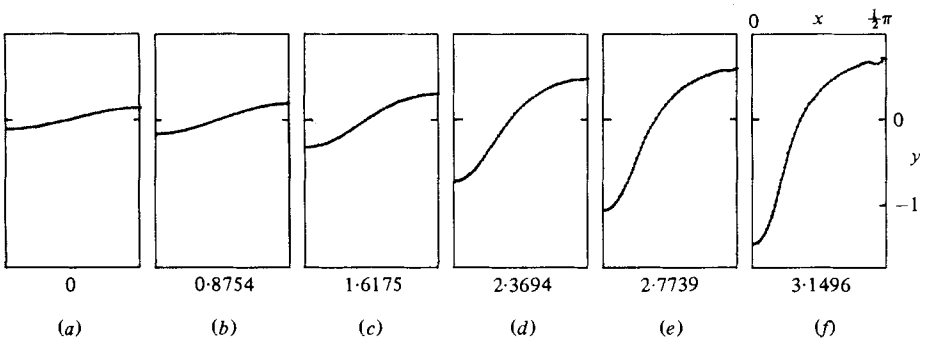

FIGURE 7. Sequence of interface profiles, $\alpha = -0{\cdot}998, F = 0, \beta = 0$. Values of $t_2 = [2|\alpha|(1-\beta^2)]^{\frac{1}{2}}t$ as shown.

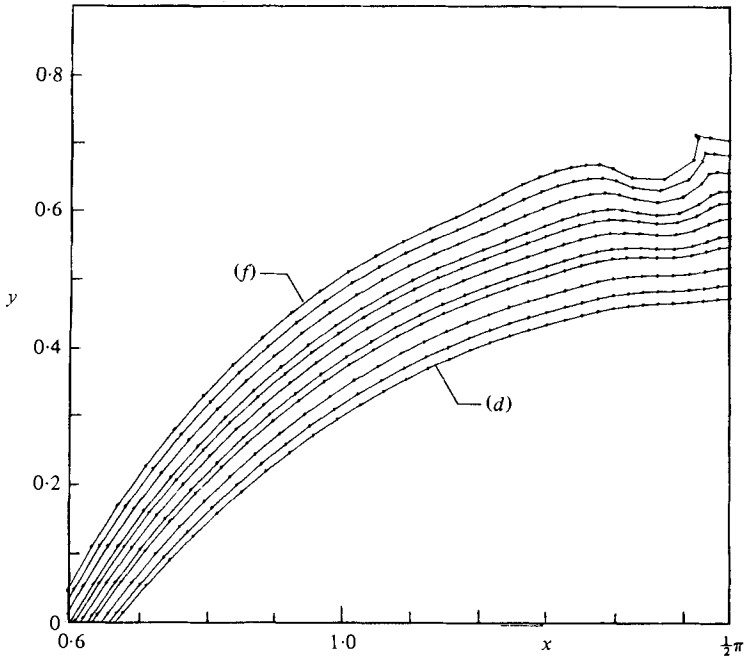

FIGURE 8. Close-up of the interface bubble profile between frames (*d*) and (*f*) of figure 7.

$x_k = (k-1)\Delta a$ $(k = 1, \ldots, N)$, where here $\Delta a = \frac{1}{2}\pi/(N-1)$, with $y(x_k, 0)$ and $\Gamma(x_k, 0)$ being obtained from (41). The motion thus starts from rest. For the computations with $\beta < 1$, the particle-velocity-weighting function was specified as $f(a) = -\cos 2a$. With this choice we are then following particles on the concave side of the interface at each of the two antinodal points (spike and bubble tips) with a smooth variation of weighting in between. Thus undesirable separation of marker particles due to stretching of C in regions of high curvature is avoided.

Figure 7 shows the unstable growth of the interface amplitude for $\alpha = -0{\cdot}998$ and $\beta = 0$, chosen to simulate zero surface tension. The value $\epsilon = 0{\cdot}125$ was used for this and most other calculations reported here since it gives approximately the same ϵ/λ ratio as in Lewis' air–water experiments. In figures 7 (*a*)–(*d*), until

$$t_2 = [2|\alpha|(1-\beta^2)]^{\frac{1}{2}}t = 2{\cdot}3694,$$

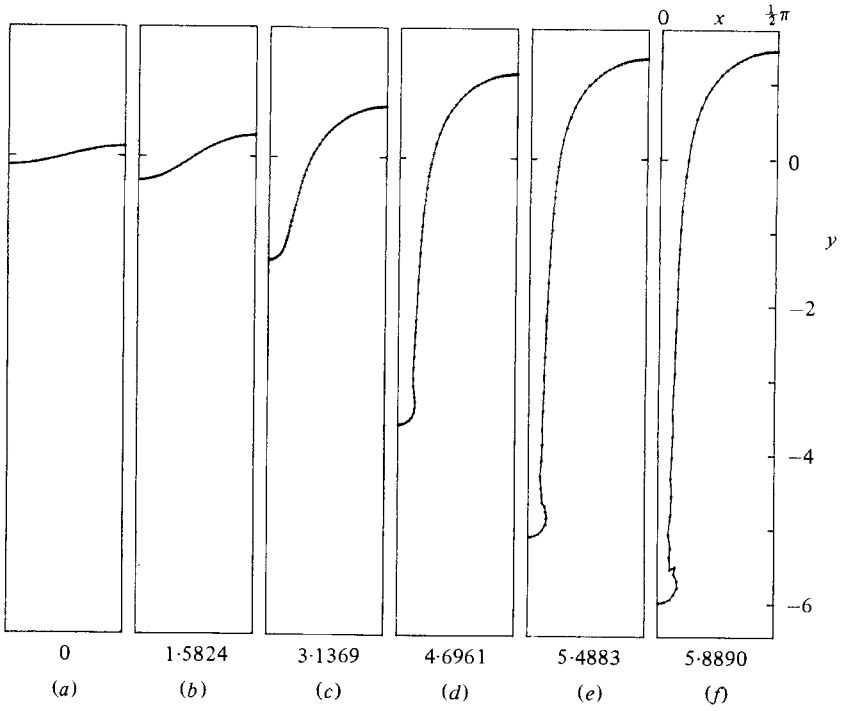

FIGURE 9. Sequence of interface profiles, $\alpha = -0{\cdot}998$, $F = 0$, $\beta = 0{\cdot}2$. Values of t_2 as shown.

the initial growth of a spike for $Y < 0$ and a bubble for $Y > 0$ can be clearly seen. The interfacial shape remains smooth up until $t_2 = 2{\cdot}7739$, at which point a small kink can be seen just to the left of the bubble tip. The details are more apparent in close-up of figure 8. A region of positive curvature develops near $a = \frac{1}{2}\pi$, which subsequently grows into a secondary Rayleigh–Taylor instability within the bubble region of the primary instability. A cusp-like feature indicating the appearance of a curvature singularity can be clearly seen in the final profile. The most likely cause of this behaviour is again a discrete form of the infinitesimal-wavelength instability predicted by Birkhoff (1962). The reason for its growth on the spatial scale shown in figures 7 and 8 is unknown. It may be due to an effective numerical surface-tension term being generated in some part of the calculation possibly in the 5-point smoothing used in the calculation of the $(\dot{z}_k, \dot{\Gamma}_k)$ set. These secondary instabilities were not seen by Baker *et al.* (1980) in their computation of the $\alpha = -1$, $\beta = 0$ case, nor did they appear after the wave had overturned in the present breaking-wave calculation of figure 1.

In the run depicted in figure 9, $\beta = 0{\cdot}2$, which corresponds approximately to the initial perturbation wavelength at the air–water interface in Lewis' experiments. There is no sign of the secondary instability near the bubble peak, so the calculation is able to proceed until in figure 9 (*e*) the spike–bubble amplitude exceeds 2 wavelengths. Note that with the choice $f(a) = 0$ (moving with the mean velocity on the interface) the calculation of figure 9 could not be extended past $t_2 = 3{\cdot}1369$ owing to stretching of interface marker points near the spike and bubble tips. Figures 9 (*d–f*) show clearly the appearance of a heavy fluid bulge due to the effect of surface tension resisting the formation of regions of very high curvature in the vicinity of the spike tip. In figures

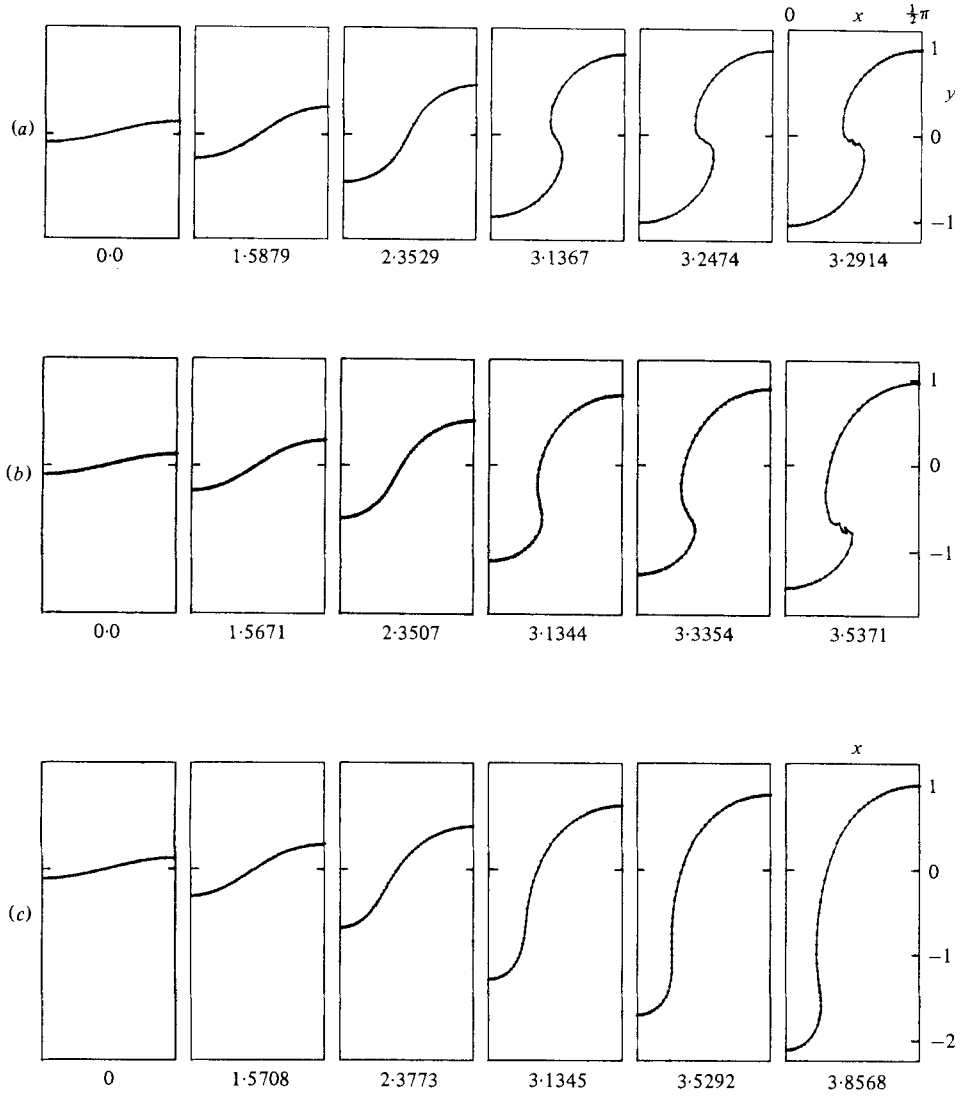

FIGURE 10. Three sequences of profiles for various α; $F = 0$, $\beta = 0{\cdot}5774$: (*a*) $\alpha = -0{\cdot}0637$, (*b*) $-0{\cdot}500$, (*c*) $-0{\cdot}998$; values of t_2 as shown.

9(*e*, *f*) the small-scale interface irregularities have developed with subsequent termination of the calculation. We mention here values of the integral invariants for the calculation λ of figure 9, which are typical of other cases with $N = 61$. Both $\bar{y}$ and Ω increased steadily from $O(10^{-6})$ in figure 9(*a*) to $O(10^{-3})$ in figures 9(*e*,*f*). In figure 9(*a*) $\Delta E = O(10^{-8})$, increasing to $O(10^{-4})$ in figure 9(*d*) and to $O(10^{-2})$ in figure 9(*f*). The corresponding values for $U_s(t) - U_s(0)$, $V(t) - V(0)$ and $T(t) - T(0)$ at frame (*f*) were respectively $O(10^{-1})$, $O(10)$ and $O(10)$, so that fractional changes remain small.

Figure 10 shows three sequences that illustrate the effect of α on the evolution of the interfacial profile for $\beta = 0{\cdot}5774$. With $\alpha = -0{\cdot}998$ the interface remains smooth with the formation of a bulge at the spike tip as for the case of figure 9. The more pronounced

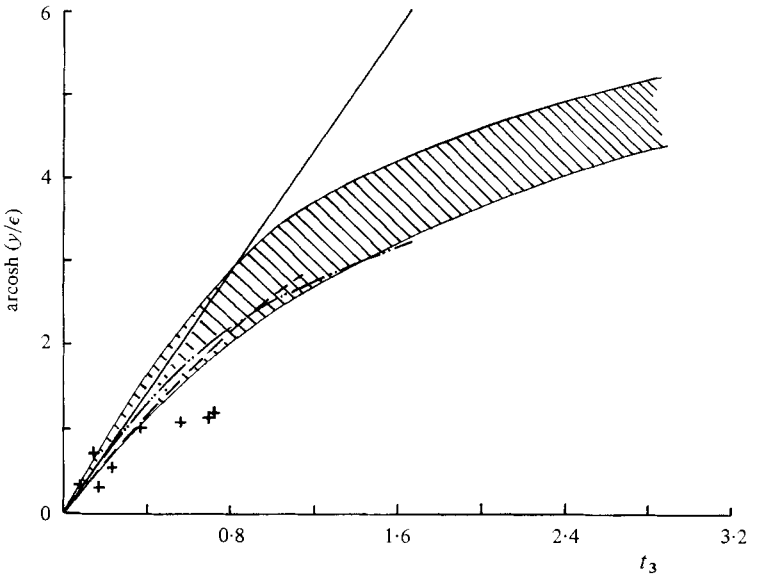

FIGURE 11. Growth of bubble amplitude compared with experimental results of Lewis (1950); ———, linear theory, $\beta = 0$; —··—, calculation, $\alpha = -0{\cdot}998, \beta = 0{\cdot}2$; — — — —, calculation, $\alpha = -0{\cdot}0637, \beta = 0{\cdot}5774$; +, benzene–water data; ▨, air–water data.

bulges of figures 10(*a*, *b*) with $\alpha = -0{\cdot}0367$ and $-0{\cdot}05$ respectively may be due to incipient Kelvin–Helmholtz instability being inhibited by the action of surface tension. The last frames of figures 10(*a*, *b*) again show the development of irregularities on the interface in regions of very high curvature where the solution is determined locally by competing inertial and surface-tension forces.

In figure 11 the growth of the bubble amplitude is plotted together with some of the experimental results of Lewis (1950), using $t_3 = (\alpha/2\pi)^{\frac{1}{2}}t$ as the time axis to allow direct comparison with figure 16 of Lewis' paper. Experiment and calculation are only in fair agreement, even taking into account the spread of air–water interface data. Lewis' experiment was very difficult to perform however and the results may suffer from a variety of systematic sources of error such as accurate determination of the apparatus acceleration (of order 20–50*g*), the initial disturbance amplitude and the mean interface level required to estimate the bubble amplitude.

6. Discussion

It seems clear from the present results that the inclusion of a surface-tension term in (19) allows the interface motion to be followed for longer periods of time, but that eventually profile irregularities appear which are not dissimilar to those observed for the ill-posed $\beta = 0$ case. Three possible sources of these difficulties are as follows:

(*a*) The presence of a surface-tension term only removes the ill-posedness for some finite initial period. Later in the highly nonlinear phase, inertial (or gravitational) effects are sufficiently strong to excite infinitesimally short perturbations locally so that ill-posedness returns. This hypothesis is contrary to the intuitive notion of surface tension (successfully) resisting the formation of interface curvature singularities with concomitant infinite pressure jumps. It is difficult to see how it could be tested by numerical means.

(*b*) The instabilities are physically based. Some evidence for this interpretation is suggested by the experiments of Thorpe (1969). Using a tilting-tank technique to generate Kelvin–Helmholtz instability for $\alpha = 0{\cdot}124$, Thorpe observed the appearance of small breaks in the two-fluid interface and the subsequent formation of drops of one fluid in the other. No smooth overturning motion was observed. Thus the irregularities may be the two-dimensional equivalent of what is in reality incipient three-dimensional drop formation. One possible mechanism for this phenomenon is Kelvin–Helmholtz/Rayleigh–Taylor instability on a scale comparable with the local arc length under conditions generated by nonlinearities. To investigate this hypothesis values of λ_s and λ_m as defined by (34)–(36) corresponding to local conditions at each point on C were calculated, taking into proper account the normal component of effective gravity and the local instantaneous velocity jump. For figure 4(*a*) at $t_1 = 1{\cdot}6697$, $\min(\delta_s) \simeq 0{\cdot}11$ and $\min(\delta_m = \pi\lambda_m/\lambda) \simeq 0{\cdot}16$, while for figure 6 at $t_1 = 1{\cdot}7309$ $\min(\delta_s) \simeq 0{\cdot}11$. For figure 9 at $t_2 = 5{\cdot}4883$ $\min(\delta_s) \simeq 0{\cdot}60$ and $\min(\delta_m) \simeq 0{\cdot}90$. Since these values are rather larger than the local arc length, we might conclude that the irregular behaviour is not due to secondary inertial/gravitational instabilities. This conclusion could be modified substantially by the effect of local interfacial compression which usually accompanied the appearance of irregular motion. Vortex-sheet compression is known to intensify linearized inertial instability in the constant density case (see Saffmann & Baker 1979) and so may well reduce the effective δ_s in the present flows.

(*c*) The irregular behaviour is a purely numerical instability, possibly a recurrence at a later time of the saw-tooth instability discussed earlier. One method of testing this hypothesis (and also (*b*)) is to improve spatial resolution through increasing N. The irregular behaviour was certainly present with $N = 45$ for the flow of figures 3 and 4 and it appeared at about the same t as for $N = 91$. Unfortunately, computational limitations restricted further significant increases in N. Some additional tests, however, were carried out for the flow of figures 3 and 4. To investigate the reliability of the predictor–corrector time-integration method, this case was recalculated using a standard fourth-order Runge–Kutta method. The results were indistinguishable graphically from those of figure 4(*a*). This case was also recalculated with 5-point linear smoothing on the (z_k, Γ_k) set every 5 time steps in addition to the smoothing discussed in §3.3. In the results displayed in figure 4(*b*), although the small-scale motions are partially attenuated, they are nevertheless present and growing in amplitude at $t_1 = 1{\cdot}6904$. Moreover, Δt has been reduced to $O(10^{-4})$, which is too small for the practical continuation of the calculation. From this example we may tentatively conclude that linearly smoothing the dependent variables is not an effective means of suppressing the appearance of small-scale profile irregularities.

Additional difficulties in the form of any of (*a*)–(*c*) above may also result from the dispersive non-dissipative nature of the surface-tension mechanism in the context of the present inviscid model. Equation (31) shows that, in the absence of viscous damping, very short capillary waves are only neutrally stable. Furthermore their phase velocity increases as $\lambda^{-\frac{1}{2}}$ when $\lambda \to 0$. It is therefore conceivable that this unphysical short-wavelength behaviour combined with the present use of periodic boundary conditions could lead to some form of spurious nonlinear dispersive reinforcement of small-scale motions, and subsequently to either the local amplification of finite length scales or in the worst case to local ill-posedness. If this were indeed the case the addition of surface tension alone could not be seen as a satisfactory means of stabilizing the interface motion.

7. Conclusions

A vortex-like description of the nonlinear motion of an interface separating two inviscid immiscible fluids of different densities has been formulated. A scheme for the numerical solution of the resulting initial-value problem has been developed and utilized to study the nonlinear behaviour of finite-amplitude normal modes of both pure Kelvin–Helmholtz and pure Rayleigh–Taylor instability. In addition to the growth of the primary instability, three types of secondary instability were identified:

(I) a saw-tooth-like instability similar to that found by Longuet-Higgins & Cokelet (1976) in their free-surface-wave studies;

(II) the development of chaotic motion among the interface-marker particles for the strong inertially driven Kelvin–Helmholtz mode and the appearance of a curvature singularity in the weaker gravitational Rayleigh–Taylor mode, for all cases in which no surface-tension term was included in the interfacial equations;

(III) the local appearance of small-scale corrugations in regions of high curvature in the interface profile.

It is almost certain that the type I behaviour results from some form of numerical instability within the discretized computational scheme. The method of partial smoothing described in § 3.3 was found to be a useful *ad hoc* means of controlling the growth of these motions in the present application, but, since the source of the instability was not discovered, there is no guarantee that it would be effective in other configurations. The present results indicate that the type II instability is the nonlinear analogue of ill-posedness of the linearized solution in the absence of surface tension and/or viscosity. The onset of this behaviour was suppressed for a finite time by the inclusion of a surface-tension term, which allowed the interface motion to be followed into the nonlinear regime, but eventually the type III instability appeared, leading to the termination of the simulation. The cause of this instability remains unknown. It could be dispersive capillary-wave phenomena that are accurately reflected in the nonlinear simulations but which are physically spurious in the absence of viscous damping. Alternatively, the instability may be a purely numerical effect that could be eliminated through analysis of the discretization procedures employed. It seems clear that the late-time irregular motion cannot be explained as straightforward inviscid Kelvin–Helmholtz or Rayleigh–Taylor instability corresponding to local conditions on the interface. There nevertheless remains the interesting possibility that the type III behaviour in some sense represents the real tendency of the interface to break up into droplets or spray through an unknown and probably nonlinear mechanism, as the flow locally undergoes transition to a (three-dimensional) turbulent mixing phase. The realistic computation of the two-fluid motion in this regime would then require some form of statistical description as the present two-dimensional inviscid model of a continuous simply connected interface is clearly inappropriate.

The author would like to thank Dr J. Y. Holyer of Topexpress Limited, who kindly supplied him with detailed solutions for interfacial gravity waves, and also Dr R. H. J. Grimshaw of the Department of Mathematics, University of Melbourne, who provided useful comments on the original manuscript.

Appendix A. Marker-particle velocity-weighting function $f(a)$

The velocities of the fluid 1 and fluid 2 on either side of $z(a,t)$ on C are given by

$$\left(\frac{dW}{dz}\right)_1 = \left(\frac{dW}{dz}\right)_p - \frac{1}{2}\left(\frac{\partial\Gamma}{\partial a}\right)\left(\frac{\partial z}{\partial a}\right)^{-1}, \tag{42a}$$

$$\left(\frac{dW}{dz}\right)_2 = \left(\frac{dW}{dz}\right)_p + \frac{1}{2}\left(\frac{\partial\Gamma}{\partial a}\right)\left(\frac{\partial z}{\partial a}\right)^{-1}. \tag{42b}$$

For $\rho_1 = \rho_2$ the standard convention has been to define the velocity of a marker particle as the mean of (42a, b). It then follows that (see §2.2)

$$\Gamma(a,t) = \Gamma(a,0), \tag{43}$$

which allows the identification of marker particles with material particles obeying Helmholtz's theorem for two-dimensional flow. Equations (9) and (10) with $f = 0$ are then a complete 'Eulerian–Lagrangian' description of the flow automatically satisfying pressure continuity at C.

It is nevertheless clear that in an inviscid fluid $C(t)$ itself is not a material curve but rather defines the instantaneous line of contact of material curves of fluid 1 and fluid 2 in local relative tangential motion. Marker particles are thus not (in general) material particles, and consequently the definition of their velocities is constrained only by the requirement of consistency with continuity of the normal component of the extended Eulerian velocity field. We may therefore define the marker-particle velocity validly according to

$$\dot{z}^* = \tfrac{1}{2}(1+f)\left(\frac{dW}{dz}\right)_1 + \tfrac{1}{2}(1-f)\left(\frac{dW}{dz}\right)_2. \tag{44}$$

If $f \neq 0$ (44) is no longer sufficient to describe $C(t)$, since (43) is not then valid. An additional equation for $\Gamma(a,t)$ is required, which is obtained in §2.2 from the pressure-continuity condition. Hence, for $\rho_1 = \rho_2$, $f = 0$ is not a necessary choice but is rather a mathematically convenient one with a somewhat misleading physical interpretation.

Now, for $\rho_1 \neq \rho_2$, $f = 0$ is no longer particularly convenient, since new circulation is continuously generated locally by buoyancy, surface-tension and inertial forces, and there is no general equivalent of (43). In a free-surface flow, for example, with $\alpha = \pm 1$ the choice $f = \pm 1$ is physically most appropriate (see Longuet-Higgins & Cokelet 1976; Baker *et al.* 1980). Indeed, in view of the aforementioned freedom in defining marker-particle velocities, there seems no reason why we should not put $f = f(a)$, provided $1 \geqslant f(a) \geqslant -1$. The study of simple special cases (e.g. a straight uniform vortex sheet with $f(a) = -\sin 2a$ shows that choice of a non-constant f can lead to problems such as marker particles converging and crossing on C. Since $|\partial z/\partial a|^{-1}$ is a measure of particle density on C, particle cross-over implies that $\partial z/\partial a = 0$ at a finite number of points. Here the sheet would develop regions of overlay in the sense that $a = a(z)$ for real a would be multiple-valued. In this event (18) and (19) should remain valid, but the present method of evaluating CPV integrals near $|\partial z/\partial a|^{-1}$ singularities would certainly have to be modified. In the present computations $\min|\partial z/\partial a|$ was estimated at each Δt to verify that practical difficulties associated with sheet overlay did not arise.

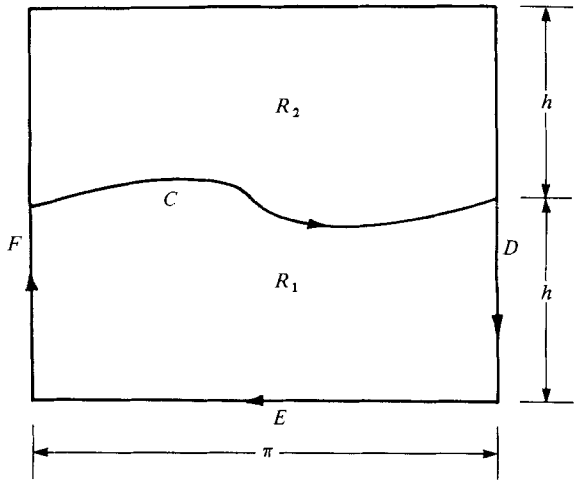

FIGURE 12. Regions R_1 and R_2 for determining x-momentum and kinetic energy; curve $L_1 = C+D+E+F$.

Appendix B. X-momentum and kinetic energy

At a time instant t, consider two strips R_1 and R_2 of the 1 and 2 fluids respectively, each of X-dimension equal to π (one wavelength) and of average Y-dimension $h \gg \pi$, as shown in figure 12. Let the boundary surrounding R_1 be the clockwise curve L_1, which we divide into segments consisting of the interface C, and straight sections D, E and F.

The total X-momentum of the fluid instantaneously in R_1 is given by

$$L_{x_1} = \rho_1 \int\int_{R_1} \left(\frac{\partial \phi}{\partial X}\right)_1 dX\, dY = \rho_1 \oint_{L_1} Y \left(\frac{\partial \phi}{\partial s}\right)_1 ds, \tag{45}$$

where the last step follows by application of Green's theorem and subsequent integration by parts. In (45) s is the arc length increasing clockwise around L_1. Writing

$$\oint_{L_1} = \int_C + \int_D + \int_E + \int_F,$$

noting that

$$\int_D = -\int_F$$

owing to the X-periodicity of the velocity field, and using an expansion of (5) for $Y \to \infty$ to evaluate $\int_E$, we find that

$$L_{x_1} = \rho_1 \int_C y \left(\frac{\partial \phi}{\partial a}\right)_1 da + \pi \rho_1 U_1 h + O(h e^{-2h}). \tag{46}$$

By an analogous argument it follows that the total X-momentum instantaneously in R_2 is

$$L_{x_2} = -\rho_2 \int_C y \left(\frac{\partial \phi}{\partial a}\right)_2 da + \pi \rho_2 U_2 h + O(h e^{-2h}). \tag{47}$$

On summing (46) and (47) the $O(h)$ terms vanish by virtue of $\rho_1 U_1 + \rho_2 U_2 = 0$ through

our choice of reference frame. Putting $\phi_1 = \overline{\phi} + \frac{1}{2}\Gamma$ and $\phi_2 = \overline{\phi} - \frac{1}{2}\Gamma$ on C, where $\overline{\phi}$ is the mean velocity potential ($\Gamma = \phi_1 - \phi_2$), and using (2) gives, as $h \to \infty$, the total X-momentum per wavelength as

$$L_x = 2\int_{-\frac{1}{2}\pi}^{\frac{1}{2}\pi} y\left(\alpha\frac{\partial\overline{\phi}}{\partial a} + \frac{1}{2}\frac{\partial\Gamma}{\partial a}\right)da. \tag{48}$$

On following a similar procedure to the above, the total kinetic energy of the fluid in R_1 may be expressed as

$$\begin{aligned} T_1 &= \tfrac{1}{2}\rho_1\int\int_{R_1}(\nabla\phi)^2\,dX\,dY \\ &= \tfrac{1}{2}\rho_1\left[\int_C \psi_1\left(\frac{\partial\phi}{\partial s}\right)_1 ds + \int_E \psi_1\left(\frac{\partial\phi}{\partial s}\right)_1 ds\right]. \end{aligned} \tag{49}$$

In establishing (49) we have applied Green's theorem and have invoked X-wise periodicity of ψ and the velocity field together with $\partial\phi/\partial n = -\partial\psi/\partial s$ on L_1 (n is the normal to L_1) and the fact that $\oint_{L_1} W\,dW = 0$. Again $\int_E$ may be evaluated using (5), so that

$$T_1 = \tfrac{1}{2}\rho_1\int_C \psi_1\left(\frac{\partial\phi}{\partial a}\right)_1 da - \frac{\pi}{2}\rho_1 U_1[f - \psi_0(t)] + \pi\rho_1 U_1^2 h + O(he^{-2h}), \tag{50}$$

where $\psi_0(t)$ is a known function arising from (5), and f is a constant. The analogous expression for the total kinetic energy in R_2 may be obtained likewise as

$$T_2 = -\tfrac{1}{2}\rho_2\int_C \psi_2\left(\frac{\partial\phi}{\partial a}\right)_2 da + \frac{\pi}{2}\rho_2 U_2[f + \psi_0(t)] + \pi\rho_2 U_2^2 h + O(he^{-2h}). \tag{51}$$

Summing (50) and (51) and utilizing $\rho_1 U_1 + \rho_2 U_2 = 0$ together with $\psi_1 = \psi_2 = \psi$ on C, we then obtain for the total kinetic energy of the fluid instantaneously in R_1 and R_2

$$\begin{aligned} T_1 + T_2 = \frac{1}{2}\int_C \psi\left[\rho_1\left(\frac{\partial\phi}{\partial a}\right)_1 - \rho_2\left(\frac{\partial\phi}{\partial a}\right)_2\right]da - \tfrac{1}{2}\pi f(\rho_1 U_1 - \rho_2 U_2) \\ + \pi h(\rho_1 U_1^2 + \rho_2 U_2^2) + O(he^{-2h}). \end{aligned} \tag{52}$$

The form of (52) indicates that as $h \to \infty$ the quantity $T_1 + T_2 - \pi h(\rho_1 U_1^2 + \rho_2 U_2^2)$ may be interpreted as that part of the total kinetic energy per wavelength associated with deviations of C from $y(a,t) = 0$. Noting that the term involving f is an absolute constant which may be neglected, we may now take the first term on the right of (52) as a quantity directly proportional to the time-varying finite part of the kinetic energy per wavelength, which, using (2), may be written as

$$T = \frac{1}{2}\int_{-\frac{1}{2}\pi}^{\frac{1}{2}\pi} \psi\left(\alpha\frac{\partial\overline{\phi}}{\partial a} + \frac{1}{2}\frac{\partial\Gamma}{\partial a}\right)da. \tag{53}$$

Equations (48) and (53) reduce to the known X-momentum and energy invariants (see Moore 1980) for $\alpha = 0$.

REFERENCES

ABRAMOWITZ, M. & STEGUN, I. A. 1972 *Handbook of Mathematical Functions*. Dover.

AHLBERG, J. H., NILSON, E. H. & WALSH, J. L. 1967 *The Theory of Cubic Splines and their Application*. Academic.

BAKER, G. R., 1980 *J. Fluid Mech.* **100**, 209–220.

BAKER, G. R. MEIRON, D. I. & ORSZAG, S. A. 1980 *Phys. Fluids* **23**, 1485–1490.

BELLMAN, R. & PENNINGTON, R. H. 1954 *Quart. Appl. Math.* **12**, 151.

BIRKHOFF, G. 1962 *Proc. Symp. Appl. Math. Am. Math. Soc.* **13**, 55–76.

CHANDRASEKHAR, S. 1961 *Hydrodynamic and Hydromagnetic Stability*. Oxford University Press.

DALY, B. J. 1967 *Phys. Fluids* **10**, 297–307.

DALY, B. J., 1969 *Phys. Fluids* **12**, 1340–1354.

FINK, P. T. & SOH, W. K. 1978 *Proc. R. Soc. Lond.* A **362**, 195–209.

GEAR, C. W. 1971 *Numerical Initial Value Problems in Ordinary Differential Equations*. Prentice-Hall.

HARLOW, F. H. & WELCH, J. E. 1966 *Phys. Fluids* **9**, 842–851.

HIRT, C. W., COOK, J. L. & BUTLER, T. D. 1970 *J. Comp. Phys.* **5**, 103–124.

HOLYER, J. Y. 1979 *J. Fluid Mech.* **93**, 433–448.

INTERNATIONAL MATHEMATICAL AND STATISTICAL LIBRARIES (IMSL) 1978 vol. 2.

KELVIN, LORD, 1910 *Mathematical and Physical Papers*, vol. 4, pp. 76–100. Cambridge University Press.

LEWIS, D. J. 1950 *Proc. R. Soc. Lond.* A **202**, 81–96.

LONGUET-HIGGINS, M. S. & COKELET, E. E. 1976 *Proc. R. Soc. Lond.* A **350**, 1–26.

MILNE-THOMSON, L. M. 1968 *Theoretical Hydrodynamics*, p. 376. Macmillan.

MOORE, D. W. 1974 *J. Fluid Mech.* **63**, 225–235.

MOORE, D. W. 1979 *Proc. R. Soc. Lond.* A **365**, 105–119.

MOORE, D. W. 1980 On the point vortex method. Preprint.

PULLIN, D. I. 1981 *J. Fluid Mech.* **108**, 401–421.

ROSENHEAD, L. 1931 *Proc. R. Soc. Lond.* A **134**, 170–192.

SAFFMAN, P. G. & BAKER, G. R. 1979 *Ann Rev. Fluid Mech.* **11**, 95–122.

TAYLOR, G. I. 1950 *Proc. R. Soc. Lond.* A **201**, 192–196.

THORPE, S. A. 1969 *J. Fluid Mech.* **39**, 25–48.

VAN DE VOOREN, A. I. 1980 *Proc. R. Soc. Lond.* A **373**, 67–91.

YIH, C-S. 1969 *Fluid Mechanics*. McGraw-Hill.

ZALOSH, R. G. 1976 *A.I.A.A. J.* **14**, 1517–1523.

ZAROODNY, S. J. & GREENBERG, M. D. 1973 *J. Comp. Phys.* **11**, 440–452.